# Numerical Simulation of Scour Around Complex Piers in Cohesive Soil

Hamn-Ching Chen[1]

## ABSTRACT

A chimera Reynolds-Averaged Navier-Stokes (RANS) method has been employed in conjunction with a scour rate equation for time-domain simulation of scour around complex piers in cohesive soils. The method solves unsteady RANS equations in a general curvilinear coordinate system using a chimera domain decomposition approach. The scour depth at each point of the streambed is determined in terms of the local shear stress using a simple scour rate equation. Calculations were performed for a model scale complex rectangular piers and a prototype circular complex pier configuration to illustrate the general capabilities of the method for prediction of combined contraction and local pier scours.

## INTRODUCTION

Scour is the erosive action of water which excavates soils from streambeds and banks. The types of scour occur at a bridge site may include general scour, contraction scour, and local scour. General scour is associated with natural processes of river flow irrespective of the presence of the bridge, whereas contraction scour and local scour are directly attributed to the presence of the bridge. Contraction scour results from river channel blockage at the bridge site and is characterized by a general lowering in the local bed elevation. Local scour is caused by the three-dimensional turbulent flow around the abutment and bridge piers, and is characterized by the formation of scour holes around the bridge foundation. The present paper is concerned with the simulation of the scour processes around complex piers including the abutment and multiple piers.

In a channel with erosive bed materials, the scour hole is formed in the vicinity of the abutment and bridge piers due to the large shear forces there. As the scour hole enlarges, the velocity near the bottom of the hole decreases gradually. When the velocity near the bottom of the scour hole decreases to a certain value, the streambed shear stresses become less than the critical shear stress necessary to initiate scour and the scour rate drops to zero. For clear-water scour, an equilibrium condition of the final scour hole will be attained if the shear stresses are below the critical shear stress everywhere in the hole.

Many parameters influence the contraction and local scours in complex pier configurations. They include fluid viscosity and density, upstream velocity, streambed

[1] Professor, Department of Civil Engineering, Texas A&M University, College Station, Texas 77843-3136, USA (hcchen@civilmail.tamu.edu)

slope and flow depth, abutment length, pier shape, pier size, flow angle of attack, and properties of the streambed soil such as plasticity, density, grain size, grain form, shear strength, cohesion, and chemical properties. In scour research, streambed soils are usually classified into cohesive soils and non-cohesive soils, although most streambed soils contain both cohesive and non-cohesive particles. Scour of cohesive soils is fundamentally different from that of non-cohesive soils. It involves more complicated physical and chemical mechanism. Once eroded, cohesive materials remain in suspension such that the clear-water scour process always prevails. Moreover, the slope of the scour hole can be very steep due to soil cohesion. In some cases, slope of 90° may be approached.

In recent years, computational fluid dynamics (CFD) has been widely used to determine fluid flow behavior in industrial and environmental applications. However, due to the complexities of both the flow field and the scour mechanism, numerical modeling of the scour process around bridge piers remains a difficult research topic. The flow field has a three-dimensional separated boundary layer flow which is accompanied by complex horseshoe vortex and wake vortex systems. During the scour process, both the horseshoe vortices and wake flows change continuously due to the continuous erosion of the streambed materials. Computation of such a transient, three-dimensional flow field requires the use of more sophisticated numerical techniques and much more computer CPU time than that of a steady flow with fixed boundaries. Particularly, erosion computation must be incorporated with the flow calculations, and grid redistribution must be performed throughout the computation to conform to the instantaneous streambed. In addition, since the flow field varies greatly close to the wall and the scour depth gradient is large around the pier, the grids ought to be sufficiently fine near the streambed and the bridge piers for accurate prediction of turbulent boundary layers and streambed shear stresses. Numerical computations of bridge pier scour were performed recently by Olsen and Melaaen (1993), Olsen (1996), Du (1997), Chen et al. (1999) and Roulund (2000), but no literature can be found for the simulation of scour around complex piers.

Recently, Chen (1995a,b) developed a multiblock RANS method for detailed resolution of the horseshoe vortex system around wing-body junctions and practical submarine configurations. The method was further extended to incorporate a chimera domain decomposition technique for time-domain simulation of ship berthing operations (Chen and Chen, 1998; Chen et al., 2000), ship roll motions (Chen et al., 2002b), and multiple ship interactions in shallow navigation channel (Chen et al., 2002a). In this study, the chimera method has been employed in conjunction with a scour rate equation for time-domain simulation of scour around complex piers in cohesive soils. Calculations were performed for two complex pier configurations with rectangular and circular piers to illustrate the capability of the chimera RANS method.

## CHIMERA RANS METHOD

In the present study, the chimera RANS method of Chen (1995a,b), and Chen et al. (1998, 2002a,b) has been extended to incorporate the scour rate equation for time-domain simulation of the scour process in cohesive soils around complex bridge piers. The

computational domain was divided into a number of smaller grid blocks, which allow complex configurations and flow conditions to be modeled efficiently through the judicious selection of different block topology and boundary conditions. The chimera domain decomposition technique was utilized to connect the overlapped or embedded grids by interpolating information across the block boundaries. The Reynolds stresses were evaluated using the two-layer turbulence model of Chen and Patel (1988). The mean flow and turbulence quantities were calculated using the finite-analytical method of Chen, Patel, and Ju (1990). The PISO/SIMPLER pressure-velocity coupling approach of Chen and Korpus (1993) and Chen and Chen (1998) was used to solve the pressure field. The scour hole shape was determined through a scour rate equation which expresses the erosion rate as a function of the streambed shear stress. More detailed descriptions of the chimera RANS method were given in Chen and Chen (1998) and Chen et al. (2002a,b).

The present method solves the dimensionless Reynolds-Averaged Navier-Stokes (RANS) equations for incompressible flow in general curvilinear coordinates $(\xi^i, t)$:

$$U^i_{,i} = 0 \tag{1}$$

$$\frac{\partial U^i}{\partial t} + U^j U^i_{,j} + (\overline{u^i u^j})_{,j} = -g^{ij} p_{,j} + \frac{1}{Re} U^i_{,jk} = 0 \tag{2}$$

where $U^i$ and $u^i$ represent the mean and fluctuating velocity components, and $g^{ij}$ is the conjugate metric tensor. $t$ is time $p$ is pressure, and Re = $U_o L/\nu$ is the Reynolds number based on a characteristic length $L$, a reference velocity $U_o$, and the kinematic viscosity $\nu$. Equations (1) and (2) represent the continuity and mean momentum equations, respectively. The equations are written in tensor form with the subscripts, $,j$ and $,jk$, represent the covariant derivatives. In the present study, the two-layer k-ε model of Chen and Patel (1988) is employed to provide closure for the Reynolds stress tensor $\overline{u^i u^j}$.

The free surface boundary conditions for viscous flow consist of one kinematic condition and three dynamic conditions. The kinematic condition ensures that the free surface fluid particles always stay on the free surface:

$$\eta_t + U\eta_x + V\eta_y - W = 0 \qquad on \quad z = \eta \tag{3}$$

where $\eta$ is the wave elevation and ($U,V,W$) are the mean velocity components on the free surface. The dynamic conditions represent the continuity of stresses on the free surface. When the surface tension and free surface turbulence are neglected, the dynamic boundary conditions reduce to zero velocity gradient and constant total pressure on the free surface. A more detailed description of the chimera RANS/free-surface method was given in Chen and Chen (1998) and Chen et al. (2000, 20002a,b).

In order to simulate the scour hole development, a scour rate equation was incorporated into the unsteady RANS method to compute the scour pattern around complex piers. For a given cohesive soil, it is known that the scour rate, defined as the change of scour depth per unit time, depends mainly on the shear stress at the streambed surface. The initiation

of the scour process is determined by the critical shear stress which represents the smallest streambed shear stress to start erosion. Based on this concept, the scour rate can be expressed as a function of the streambed shear stress and the critical shear stress. The scour rate equation can be written in the following dimensional form

$$\dot{Z} = \dot{Z}(\tau_b, \tau_c); \quad \tau_b = \mu \frac{\partial q}{\partial n} \tag{4}$$

where $\dot{Z}$ is the scour rate, $\tau_b$ is the streambed shear stress, $\tau_c$ is the critical shear stress, $q = \sqrt{U^2 + V^2 + W^2}$ is the magnitude of flow velocity, $\mu$ is the dynamic viscosity of water, and $n$ is the normal distance from the streambed. After the flow field is obtained, the soil erosion rate at each grid point on the streambed is determined by the scour rate equation. The increase of scour depth is then evaluated by multiplying the scour rate by the time increment. In the present study, the scour rate is assumed to be linearly proportional to the streambed shear stress as follows:

$$\dot{Z} = \begin{cases} c(\tau_b - \tau_c), & \tau_b > \tau_c \\ 0, & \tau_b \le \tau_c \end{cases} \tag{5}$$

The above equation has been incorporated into the chimera RANS code to facilitate the simulation of scour hole developments. During each time step, the incremental scour depths at each streambed point were computed using the scour rate equation. After the new scour depth distribution was obtained, the coordinate of each bed point was updated and the streambed was moved to the new elevation. The numerical grids were then adjusted vertically to conform to the updated bathymetry of the scoured streambed.

## RESULTS AND DISCUSSION

Numerical simulations have been performed first for a complex pier configuration with abutments and four rectangular piers as shown in Figure 1. The present configuration is identical to that tested by Li (2002) at Texas A&M University except that the water depth was reduced from 20 cm to 12 cm. The channel width upstream and downstream of the bridge is $B_1$ = 1.5 m. Each abutment is 0.48 m long and 0.06 m wide. Four rectangular piers of 0.02 m × 0.06 m were placed between the abutments with uniform pier spacing of 0.108 m. The blockage by the abutments and the bridge piers reduces the effective channel width to $B_2$ = 0.46 m with a large channel contraction ratio of $B_1/B_2$ = 3.26. A uniform upstream velocity of 0.2 m/s was used in the present simulation. To reduce the CPU time and memory requirement, the computations were performed for one-half of the solution domain and the flow was assumed to be symmetric along the channel centerline. The solution domain was divided into 8 computational blocks with a total of 508,710 grid points. An overlap region was added to all interior block boundaries to ensure the complete continuity of the solutions between adjacent grid blocks. The numerical grids were adjusted to follow both the exact free surface and instantaneous streambed elevations at every time step.

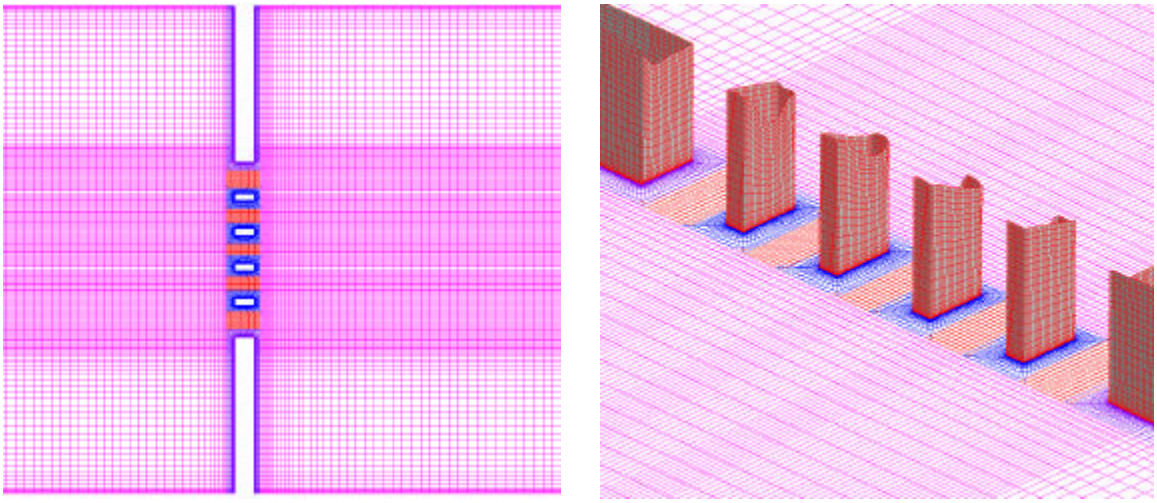

Figure 1. Bridge configuration and numerical grid for complex rectangular piers

Computations were performed first for flat bed configuration without erosion (i.e., $\boldsymbol{c} = 0$ in equation (5)) until the steady state is attained. Figure 2 shows the water elevation profiles under steady flow conditions. It is seen that there is a significant drop in free surface elevation between the piers. The highest water elevation upstream of the pier is about 1.15 cm above the mean water level, and the lowest water elevation was seen along the inner side of the two outer piers with an elevation of –3.3 cm from the mean water surface. The change in water elevation is quite significant comparing to the total water depth. However, the free surface effect was observed to diminish gradually in the flume test as the scour hole develops and the channel deepened.

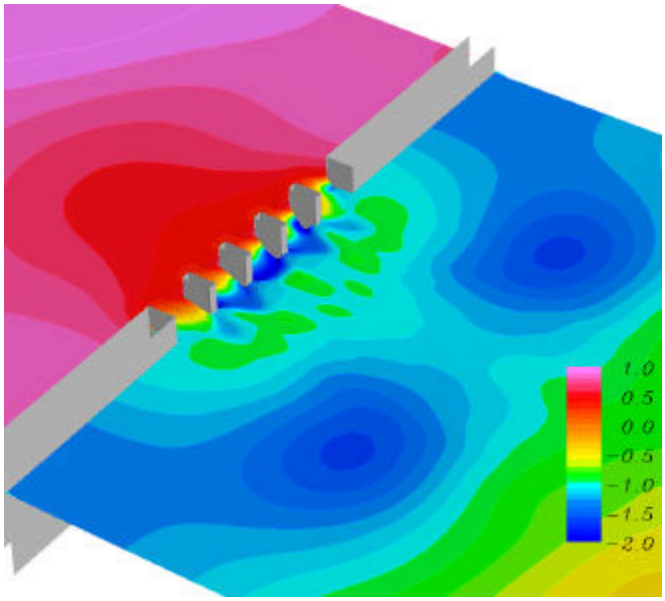


Figure 2. Free surface elevation contours around the bridge

In addition to the rather significant change in free surface elevations, the abutments and bridge piers also produce strong flow accelerations as seen in Figure 3 as a result of the narrowing of channel cross section at the bridge location. The strongest acceleration was observed between the bridge piers with a maximum velocity of nearly 0.852 m/s or 4.26 times of the upstream flow velocity. It is also noted that the stream flow separated behind the abutments and formed a pair of large recirculation regions. In addition, smaller regions of flow reversal were also observed in the wake of each pier.

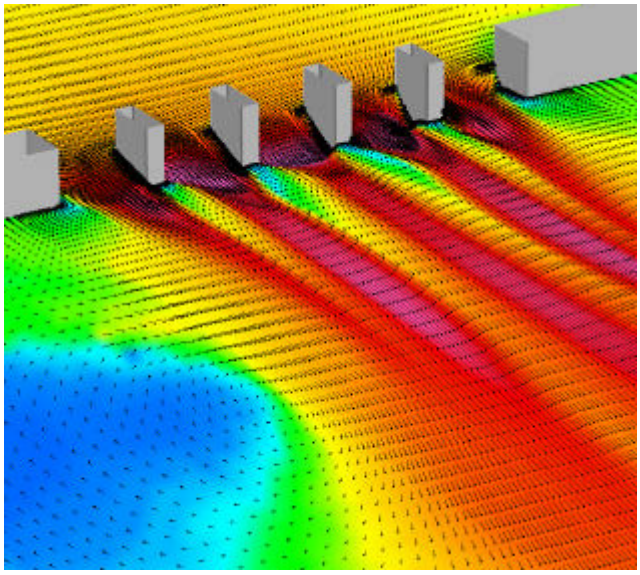

Figure 3. Free surface velocity field in the vicinity of piers

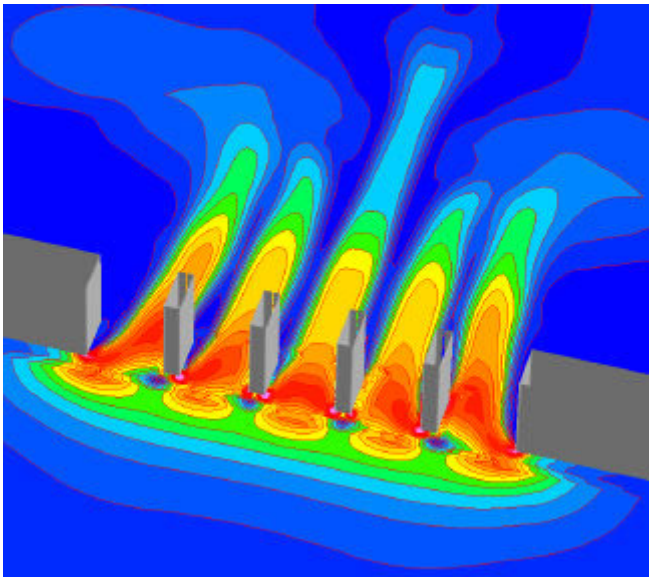

Figure 4. Shear stress distribution before scour initiation

As noted earlier, the shear stresses were computed directly from the velocity gradients on the streambed surface using eq. (4). Figure 4 shows the initial shear stress distribution

before the scour take place. It is quite clear that the shear stresses are high in the middle of each passage since the flow was forced to accelerate between the piers, and between the abutments and piers. A detailed examination of the streambed shear stresses indicated that the maximum shear stress occurs at the front corner of each abutment and around the inner front corner of each rectangular pier. It is also interesting to note that the mainstream flow approached the outer two piers with a large angle of attack. The flow angle of attack is considerably smaller for the inner two piers since the flow in the middle section of the channel is nearly parallel to the channel bank. As noted earlier, erosion occurs in the regions where the bed shear stress is greater than the critical shear stress. Therefore, the size and shape of the scour hole is expected to be dependent upon the critical shear stress as well as the streambed shear stresses.

After successful simulation of the complex pier flow for a flat streambed, the present method was coupled with the scour rate equation to predict the contraction and local scour due to complex piers. For simplicity, the free surface effects were ignored in the present simulation of complex pier scour. This is a reasonable approximation since the water depth is rather deep comparing to the pier size and the free surface does not significantly influence the scour depth. As noted earlier, the critical shear stress determines both the initiation and the end of the scour process. For accurate simulation of the scour hole development, it is necessary to determine the scour rate vs. shear stress curve from the measurement. Since neither the critical shear stress nor the scour rate was available, we will use a simple scour rate equation to illustrate the capability of the present method. In the present simulation, the dimensionless critical shear stress was chosen to be $\tau_c/\rho U_0^2 = 0.015$ which corresponds to a $\tau_c$ value of 0.6 N/m$^2$. The slope of the scour rate vs. shear stress curve was assumed to be $c$ = 0.006 m$^3$/(N·hr). Simulations were performed for 6000 time steps using a constant time increment of $\Delta t$ = 150 sec. It should be noted that the maximum initial shear stress is 4.3 N/m$^2$, or about 7 times of the critical shear stress, at the beginning of the scour processes.

In order to facilitate a detailed examination of the scour hole development and the associated shear stress variations, the numerical solution for the entire streambed was saved in a movie file at a 25 min interval (i.e., every 10 time steps). Figure 6 shows the predicted scour pattern and the corresponding shear stress distributions (normalized by $\rho U_0^2$ = 40 N/m$^2$) at 12 selected time instants. It is clearly seen that the scour was initiated in the high shear stress regions between the piers and gradually propagates towards the downstream and upstream of the bridge. For the first several hours, the scour hole in each passage develops almost independently while very little erosions were observed behind the abutments and piers. It is noted that there are five separate valleys downstream of the bridges until t = 1,000 min. During the initial stage of scour hole development, the shear stress dropped very quickly as the valleys deepened gradually. The high shear stress region was shifted gradually to the middle passage while the streambed shear stress becomes quite low in the two outermost passages. This clearly indicated that more water was flowing through the middle section of the channel while the flow rate in the outer passages was significantly reduced.

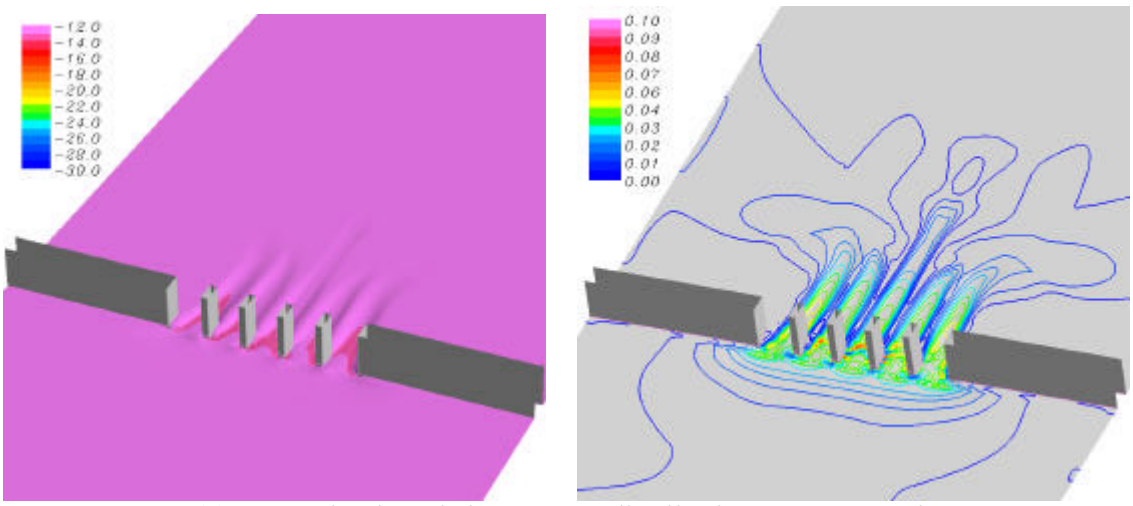


(a) Scour depth and shear stress distributions at t = 25 min

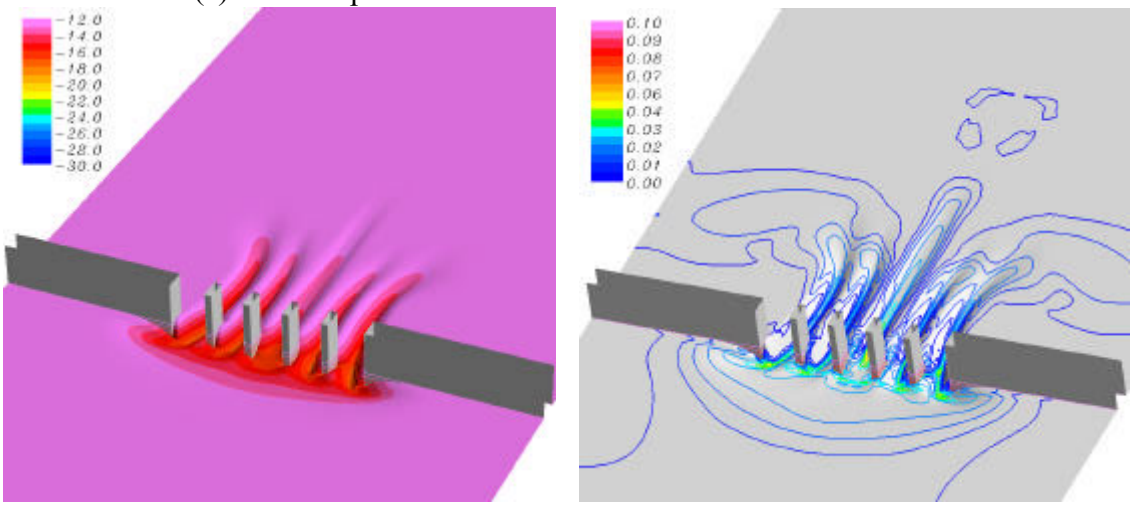


(b) Scour depth and shear stress distributions at t = 500 min

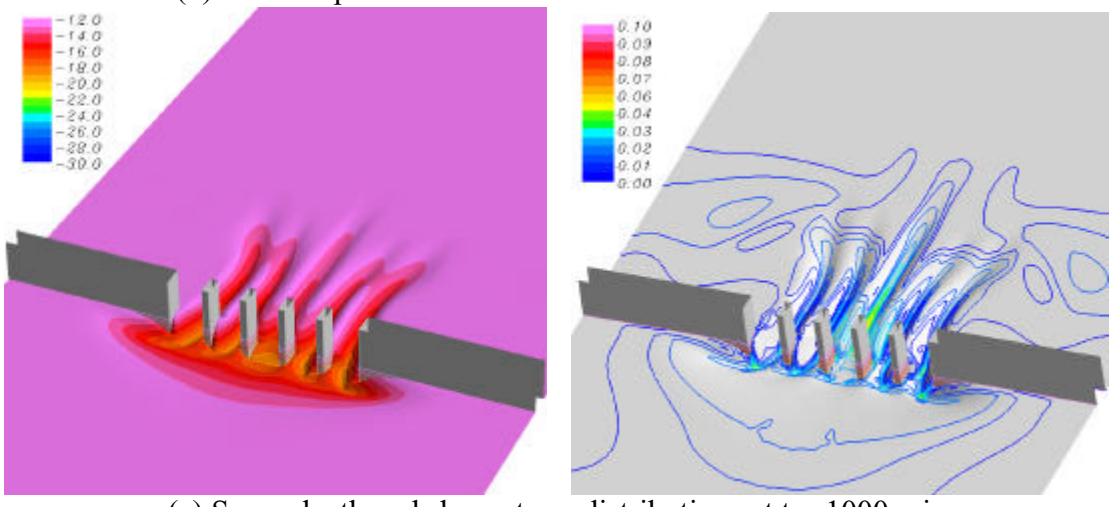


(c) Scour depth and shear stress distributions at t = 1000 min

Figure 5. Predicted scour hole shape and streambed shear stresses around complex rectangular pier configuration: (a) t = 25 min, (b) t = 500 min, (c) t = 1000 min

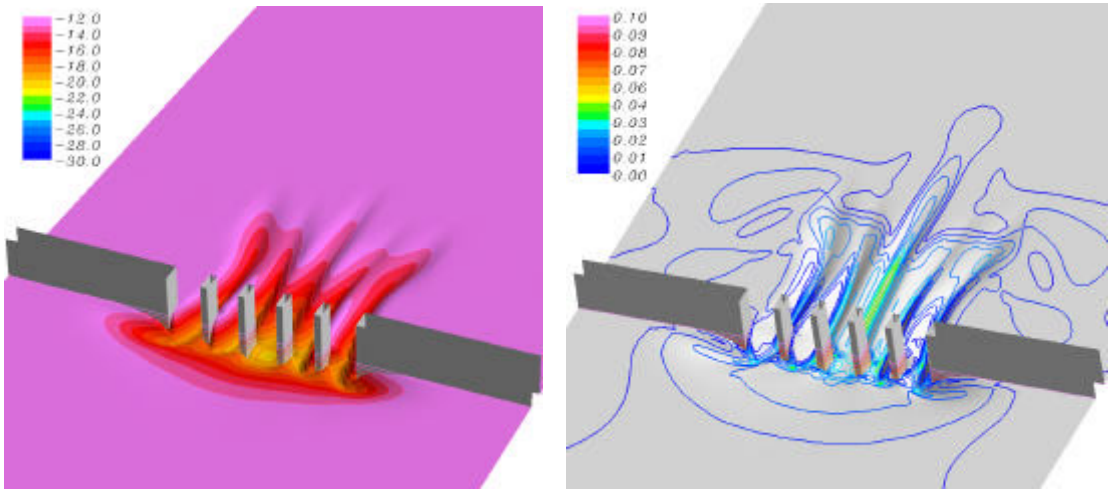


(d) Scour depth and shear stress distributions at t = 1500 min

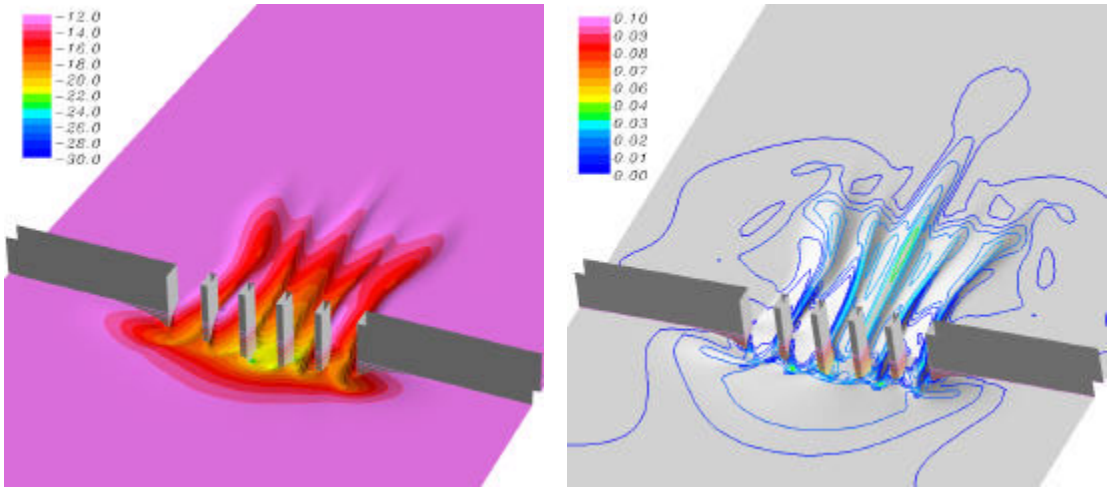


(e) Scour depth and shear stress distributions at t = 2000 min

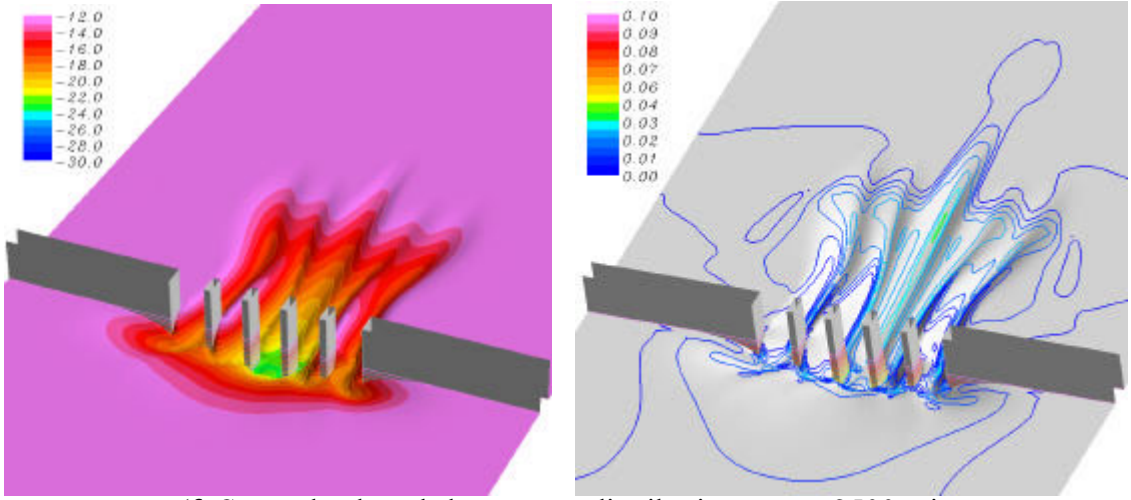


(f) Scour depth and shear stress distributions at t = 2500 min

Figure 5. Continued: (d) t = 1500 min, (e) t = 2000 min, (f) t = 2500 min

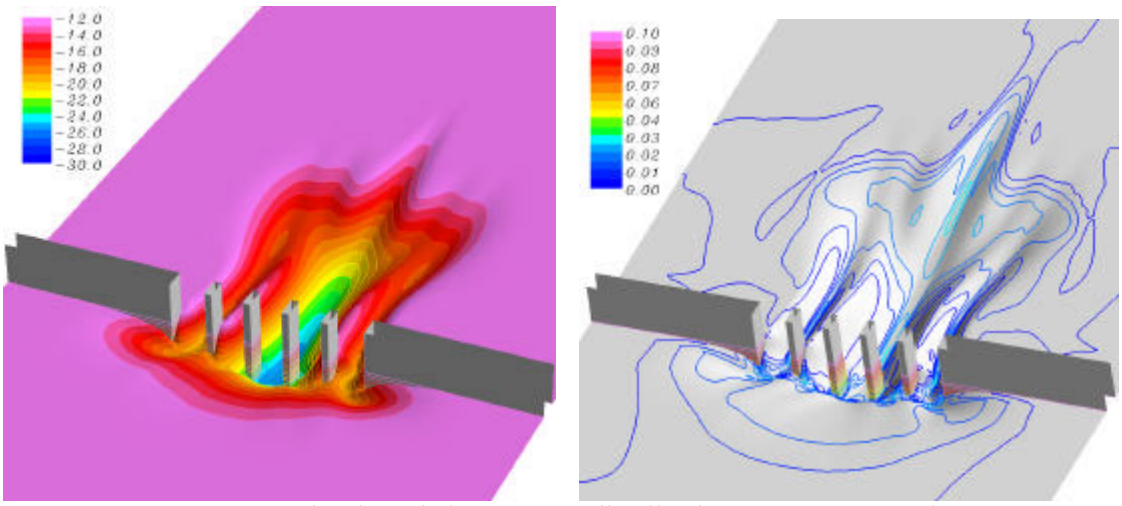


(g) Scour depth and shear stress distributions at t = 3750 min

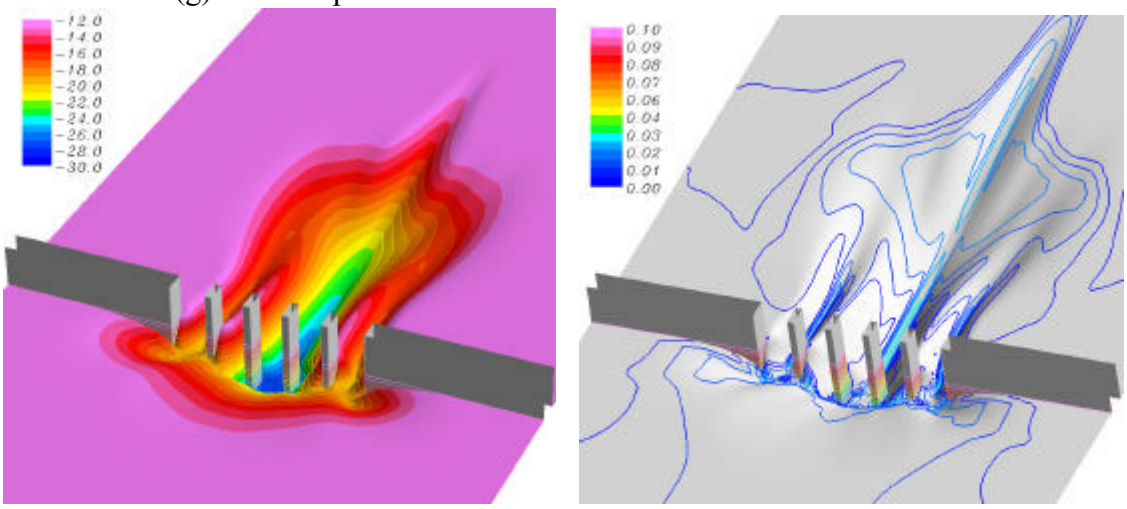


(h) Scour depth and shear stress distributions at t = 6000 min

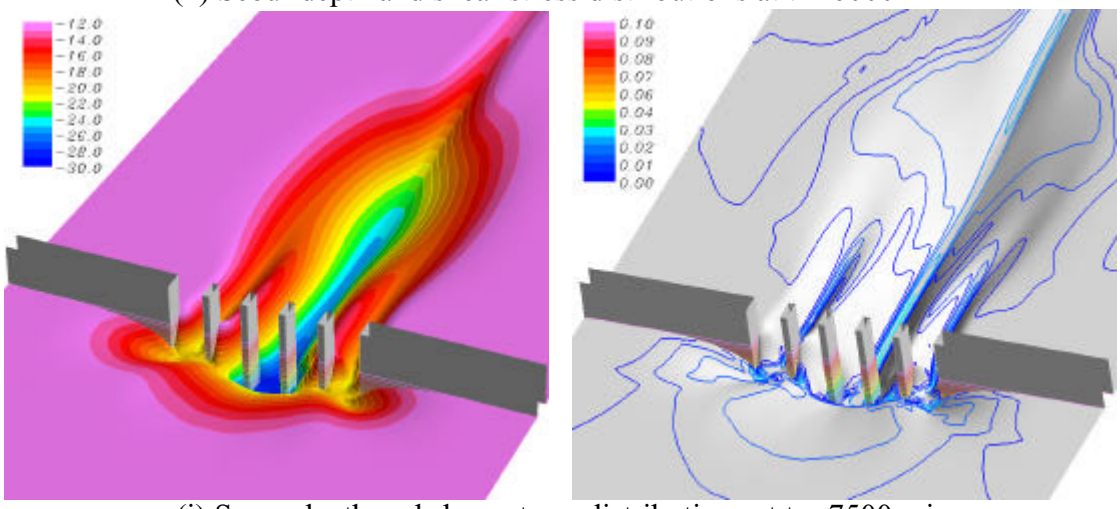


(i) Scour depth and shear stress distributions at t = 7500 min

Figure 5. Continued: (g) t = 3750 min, (h) t = 6000 min, (i) t = 7500 min

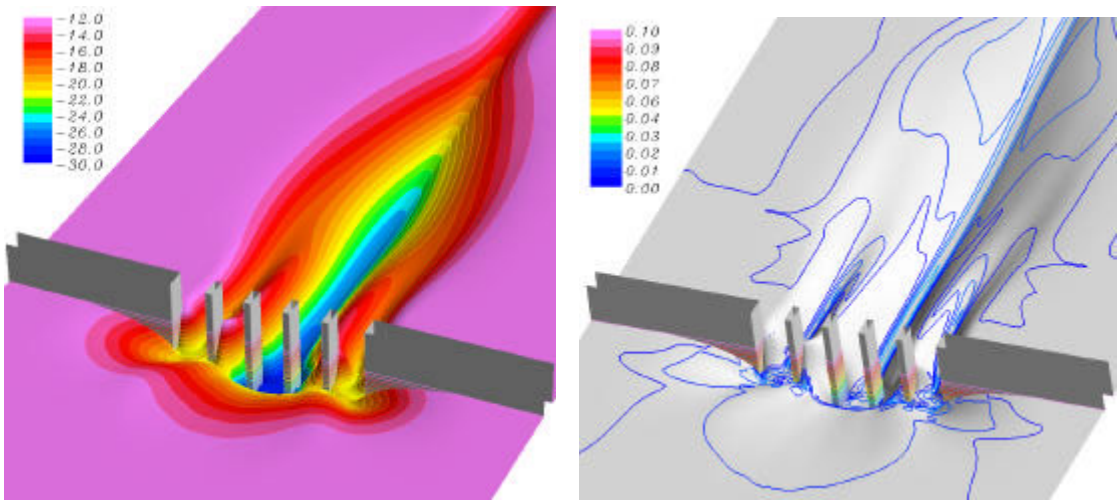


(j) Scour depth and shear stress distributions at t = 10000 min

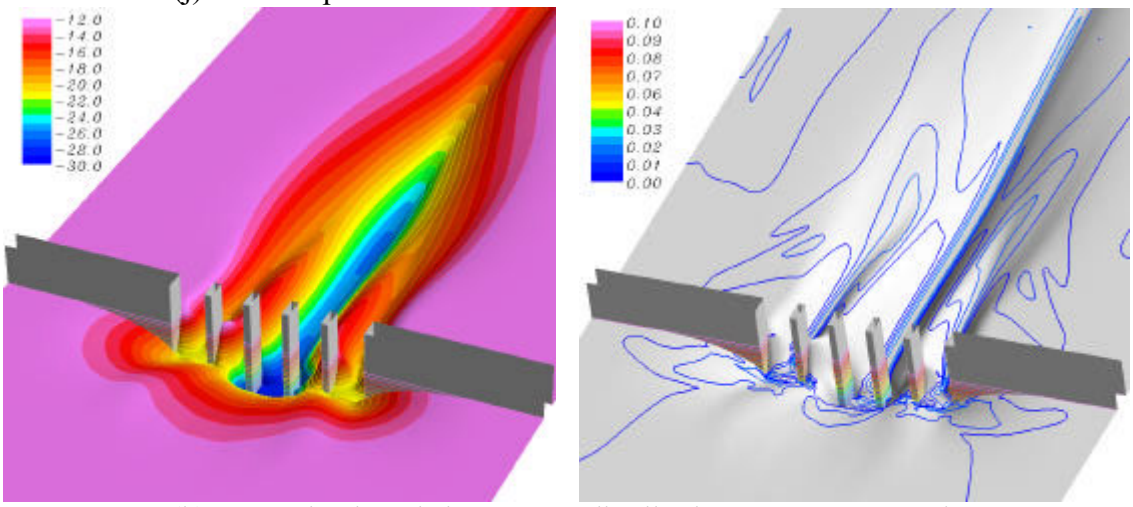


(k) Scour depth and shear stress distributions at t = 12500 min

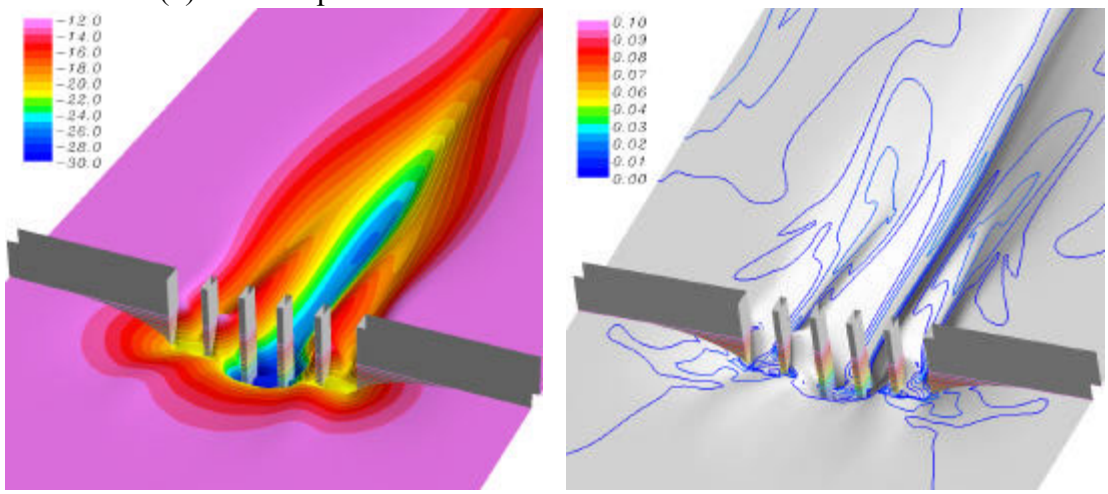


(l) Scour depth and shear stress distributions at t = 15000 min

Figure 5. Continued: (d) t = 10000 min, (e) t = 12500 min, (f) t = 15000 min

After about t = 20 hr, the ridges behind the piers also began to erode as the valleys deepened and widened continuously. As a result of this ridge erosion, the deep valleys merged into a large scour hole downstream of the pier. It is quite clear that the erosion between two central piers is significantly faster than the neighboring areas surrounding the outer piers and the abutments. Beyond t = 7,500 min, most of the new erosion took place near the middle section of the channel with only minor additional scour around the outer two piers and the abutments. The scour hole between the two inner piers continued to lengthen until about t = 12,500 min. At the end of the simulation (i.e., t = 15,000 min), the maximum shear stress reduces to about 0.91 $N/m^2$ and the deepest scour hole is about –22.7 cm (–34.6 cm below the free surface) or nearly twice of the water depth. The deepest scour hole was located on the outer back corner of the two inner piers and was produced by a combination of the contraction scour between the piers and the local scours around the piers.

Finally, we shall examine also the horseshoe vortex systems for complex pier configurations. Figure 6 shows the horseshoe vortices around the pier and the abutment at t = 12,500 min. It should be noted that the flow around the piers and abutments are highly three-dimensional with large lateral velocity components. In order to facilitate the visualization of horseshoe vortex systems, it is desirable to plot only the horizontal and vertical velocities while suppressing the lateral velocity components as shown in Figure 6. It is clearly seen that there is a large horseshoe vortex in front of the abutment. A smaller horseshoe vortex was also observed in front of the pier. As the scour hole size increases, the extent of the horseshoe vortex also increases. However, the strength of the horseshoe vortex decays gradually since the stream flow slows down at the bridge location as the scour hole was enlarged.

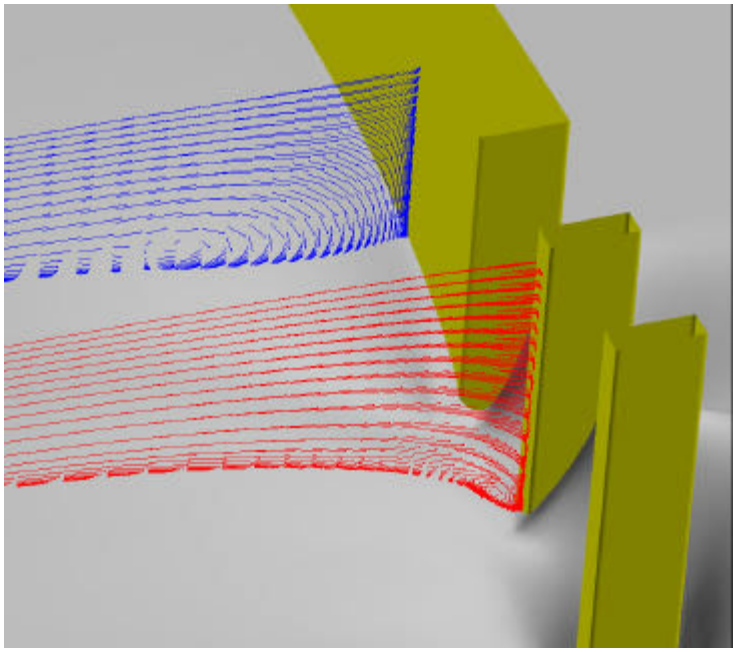

Figure 6. Horseshoe vortices around the pier and abutment

In order to further evaluate the capability of the present method, simulations were also performed for another complex pier configuration at full scale as shown in Figure 7. In this case, the channel width is 200 m and the length of each abutment is 50 m. Instead of the rectangular piers considered earlier, four circular piers of 4-m diameter each were placed between the abutments with uniform pier spacing of 20 meters. The water depth was chosen to be 12 m and the approach flow velocity was assumed to be 1 m/s. In order to reduce the CPU time and memory requirements, the computations were performed for only one-half of the solution domain with the symmetry conditions applied along the centerline of channel. The solution domain was divided into 6 computational blocks with a total of 579,847 grid points. It is noted that the cylindrical pier grid blocks were completely embedded in the rectangular channel grids using a chimera domain decomposition approach. This enables us to simplify the grid generation process and improve the resolution of turbulent boundary layers and wakes around the piers. When the streambed was eroded due to contraction and/or local scour, the numerical grids were redistributed in the vertical direction to conform to the new streambed elevation.

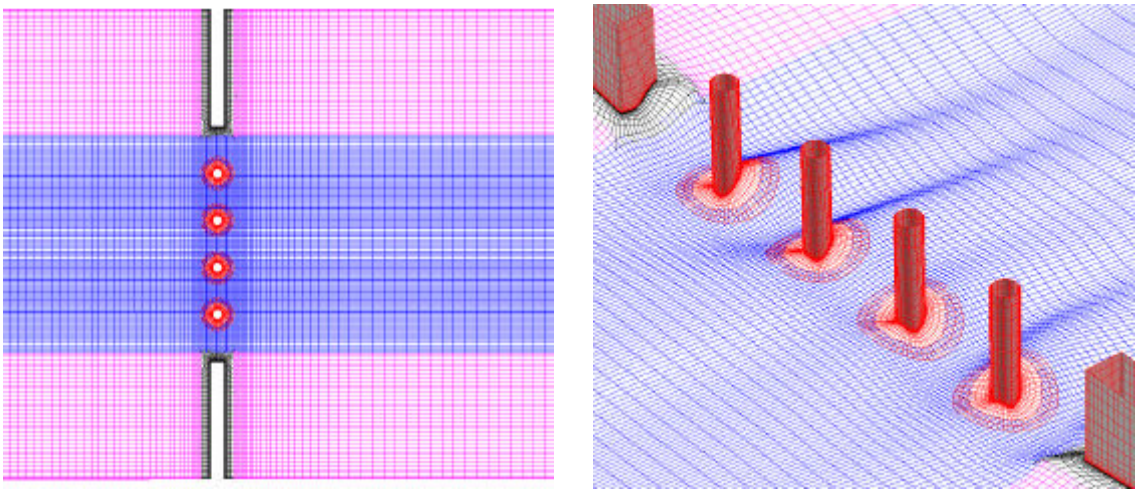

Figure 7. Bridge geometry and numerical grids for complex circular piers

Computations were performed first for the flat bed configuration without erosion until the steady flow condition is attained. For simplicity, the free surface effects were neglected. It is anticipated that the free surface may have only minor influence on the scour pattern since the water depth is quite large compared to the pier diameter. Figure 8 shows the predicted velocity distributions at the mean water surface. It is seen that the abutments and bridge piers produced strong flow accelerations at the bridge location similar to those observed in the previous case. The strongest acceleration was observed in the middle section downstream of the bridge piers. The maximum velocity was nearly 3.2 m/s or 3.2 times of the upstream flow velocity. This flow acceleration is somewhat lower than that shown in previous case since the contraction ratio due to the abutments and piers is only 2.27:1. There are again two large recirculation regions behind the abutment while the mainstream was directed towards the middle section of the channel. It is also clearly seen that the stream flow approaches the outer two piers at a fairly large skew angle.

The angle of the attack for the two central piers are considerably smaller and the wakes behind these piers are nearly parallel to the channel bank.

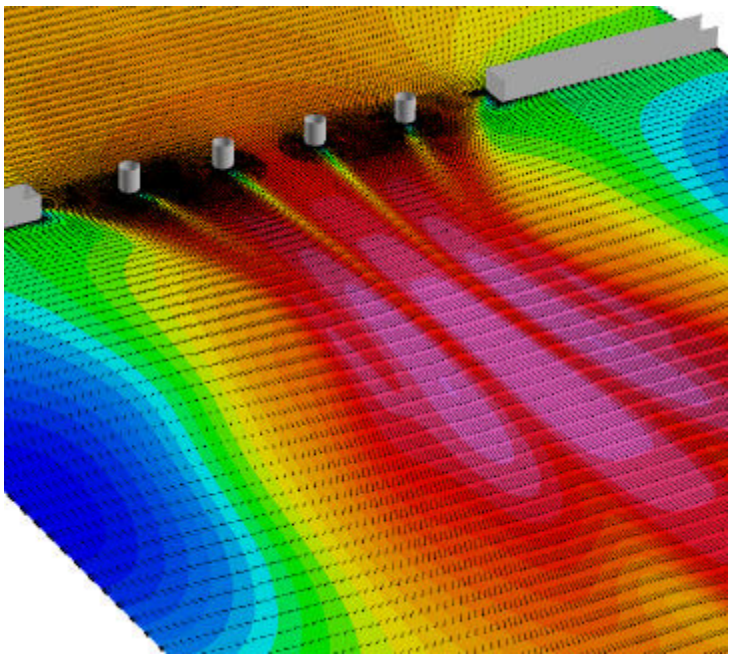

Figure 8. Free surface velocity field around complex circular pier configuration

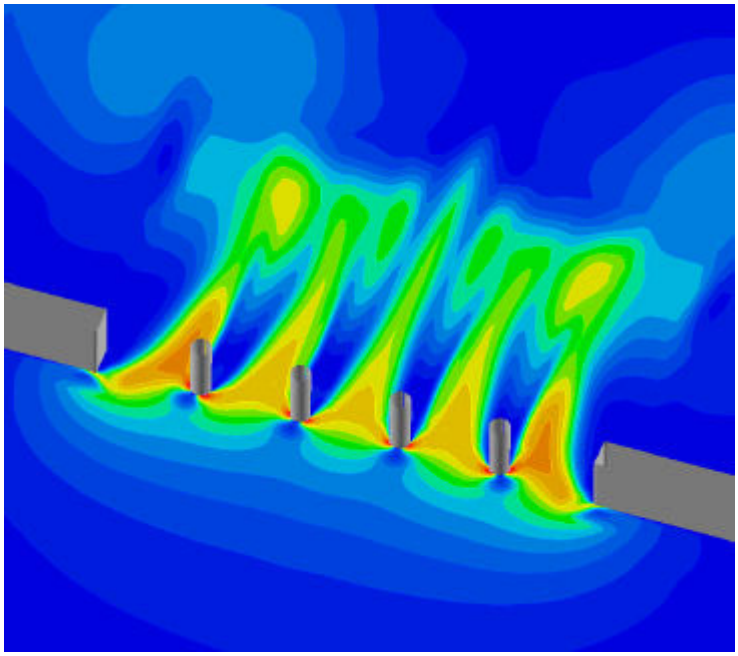

Figure 9. Shear stress distribution at the scour initiation

Figure 9 shows the initial shear stress distribution before the scour take place. It is quite clear that the shear stresses are high in the middle section of each passage since the flow

was forced to accelerate between the piers, and between the abutments and piers. The maximum shear stress was about 20.2 N/m$^2$. This is significantly higher than those predicted earlier for model scale piers because the upstream flow velocity is much higher for the present full-scale simulation. It is noted that the wakes behind the circular piers are significantly wide than those observed earlier for slender rectangular piers. The wider wakes was caused by the earlier separation of boundary layer flow around the circular pier. For slender rectangular piers, the flow separates nearly the leading corners, but tends to reattach in the middle section of the pier surface before separating again nearly the back face of the pier.

After the steady-state solution was obtained, the scour process was initiated using a critical shear stress of 1.0 N/m$^2$ (i.e., $\tau_c/\rho U_0^2 = 0.001$). The slope of the scour rate vs. shear stress curve was assumed to be $c$ = 0.006 m$^3$/(N·hr). Simulations were performed for 6000 time steps using a constant time increment of $\Delta t$ = 0.1 hr. As noted earlier, the maximum shear stress is about 20.2 N/m$^2$ or about 20 times of the critical shear stress, at the initiation of scour processes.

In order to facilitate a detailed examination of the scour hole development and the associated shear stress variations, the numerical solution for the entire streambed was saved in a movie file at a 1.0 hr interval (i.e., every 10 time steps). Figure 10 shows the predicted scour pattern and the corresponding shear stress distributions (normalized by $\rho U_0^2$ = 1,000 N/m$^2$) at 9 selected time instants. It is clearly seen that the scour was initiated in the high shear stress regions between the piers and gradually propagates towards the downstream and upstream of the bridge. During the initial stage of streambed erosion, the scour hole in each passage develops almost independently with five separate valleys downstream of the bridges. As time increases, however, the scour hole shape develops in a very different manner comparing to that seen earlier for the rectangular piers. More specifically, the scour hole not only expands in the longitudinal direction, but also extends laterally toward the channel bank with a pair of deep scour holes behind the abutments. This may be attributed, at least in part, to the relatively short abutment which enables the mainstream flow to impinge on the bank and produce a strong recirculation flow region near the channel bank. The combination of short abutment length and high streambed shear stresses produced a much wider scour hole for the prototype configuration.

A detailed comparison of the scour hole patterns for the rectangular and circular pier configurations indicated that the location of the deepest scour hole depends strongly on the complex pier configurations. For the model scale rectangular piers, the maximum scour depth was observed around the two middle piers due to combined contraction and local scours. For the prototype circular piers, however, the maximum scour occurs much farther downstream of the bridge and away from the channel centerline. The local scour around the piers and abutments were relatively small comparing to the contraction scour. It is quite clear that the scour hole development for the present circular pier configuration is dominated by the contraction scour.

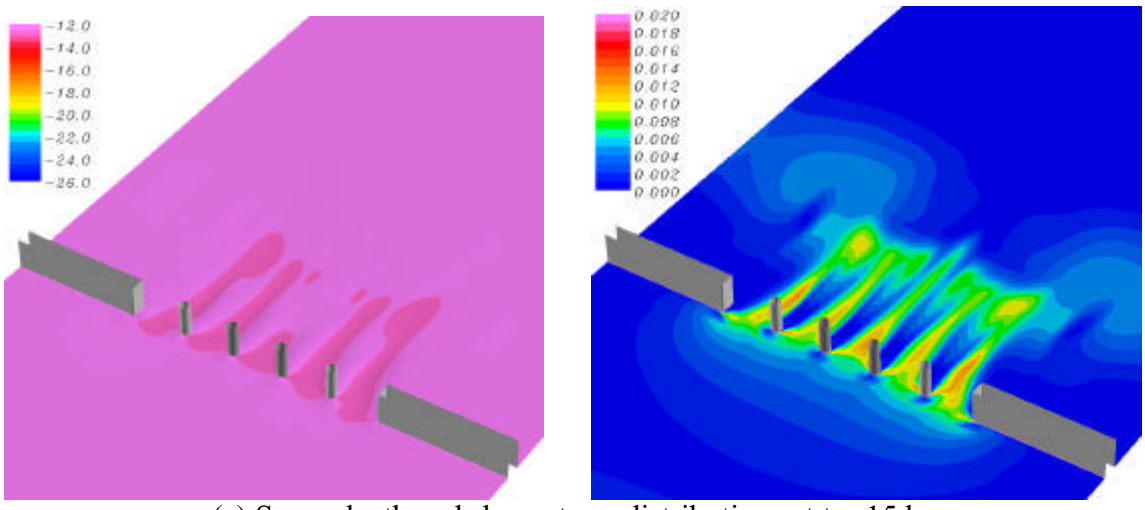


(a) Scour depth and shear stress distributions at t = 15 hr

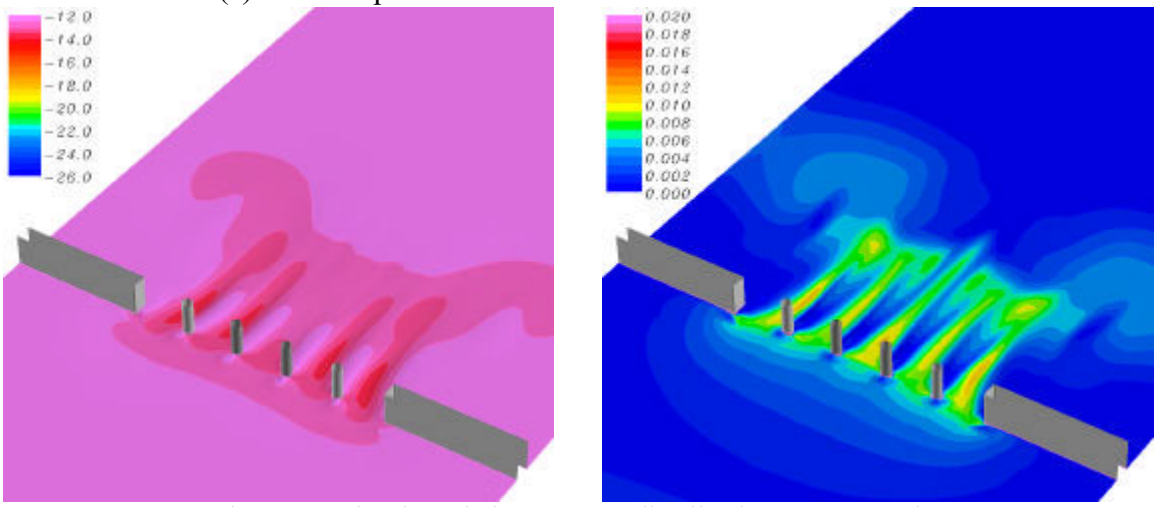


(b) Scour depth and shear stress distributions at t = 30 hr

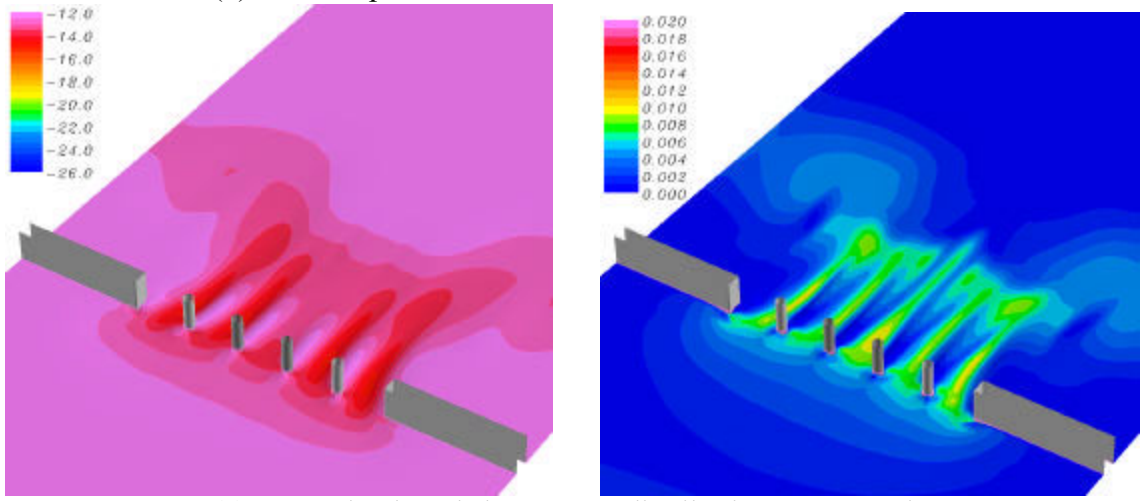


(c) Scour depth and shear stress distributions at t = 50 hr

Figure 10. Predicted scour hole shape and streambed shear stresses around complex circular pier configuration: (a) t = 15 hr, (b) t = 30 hr, (c) t = 50 hr

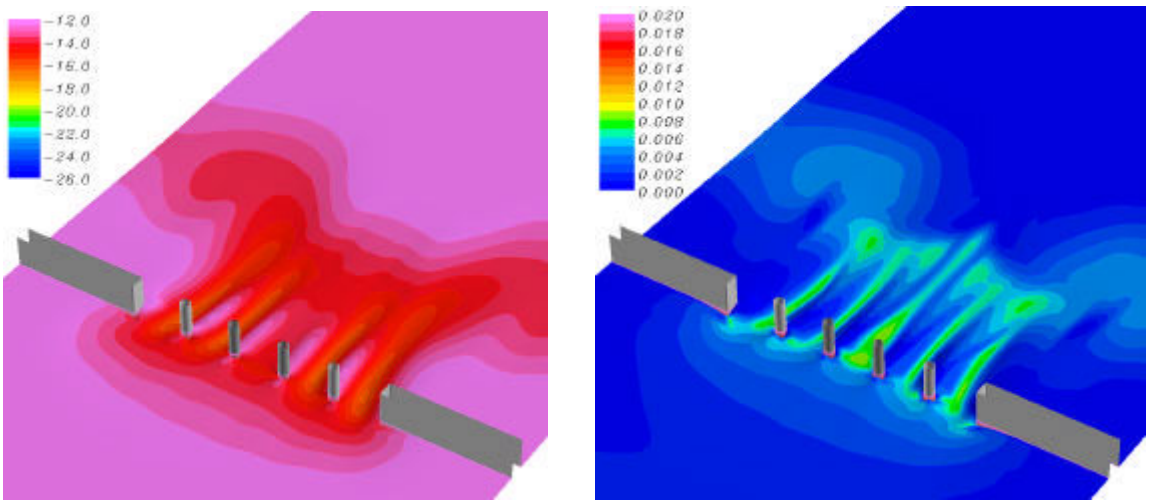


(d) Scour depth and shear stress distributions at t = 100 hr

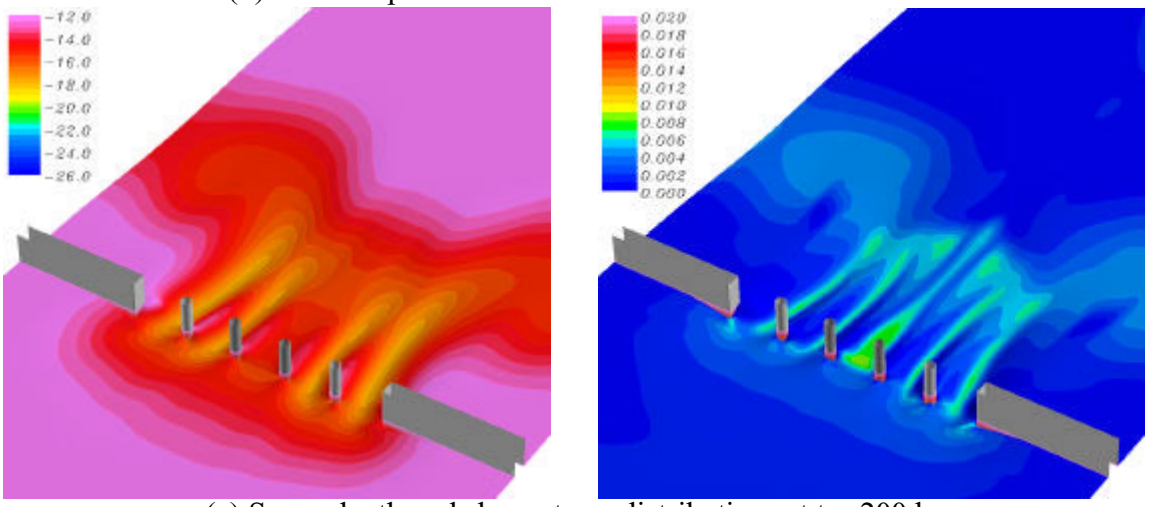


(e) Scour depth and shear stress distributions at t = 200 hr

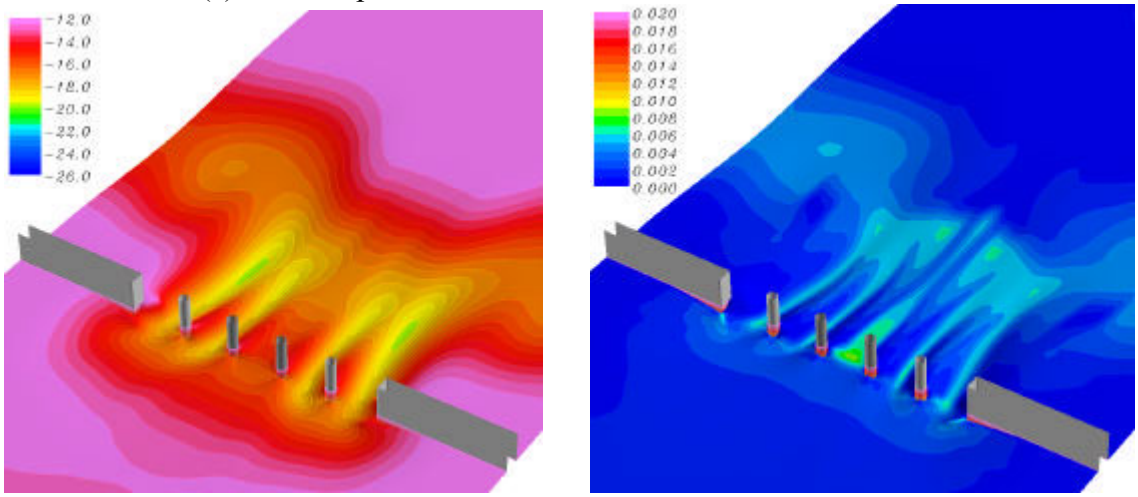


(f) Scour depth and shear stress distributions at t = 300 hr

Figure 10. Continued: (d) t = 100 hr, (e) t = 200 hr, (f) t = 300 hr

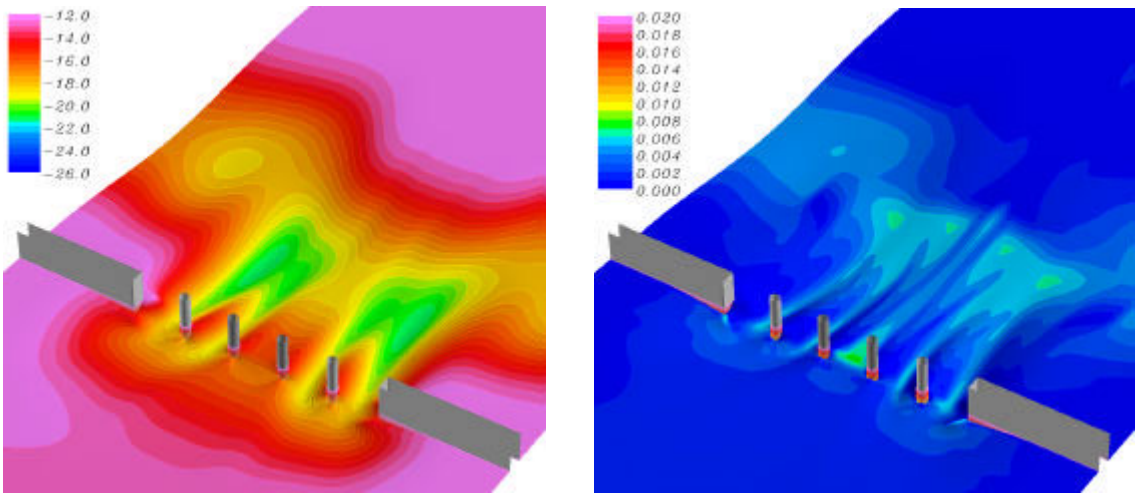


(g) Scour depth and shear stress distributions at t = 400 hr

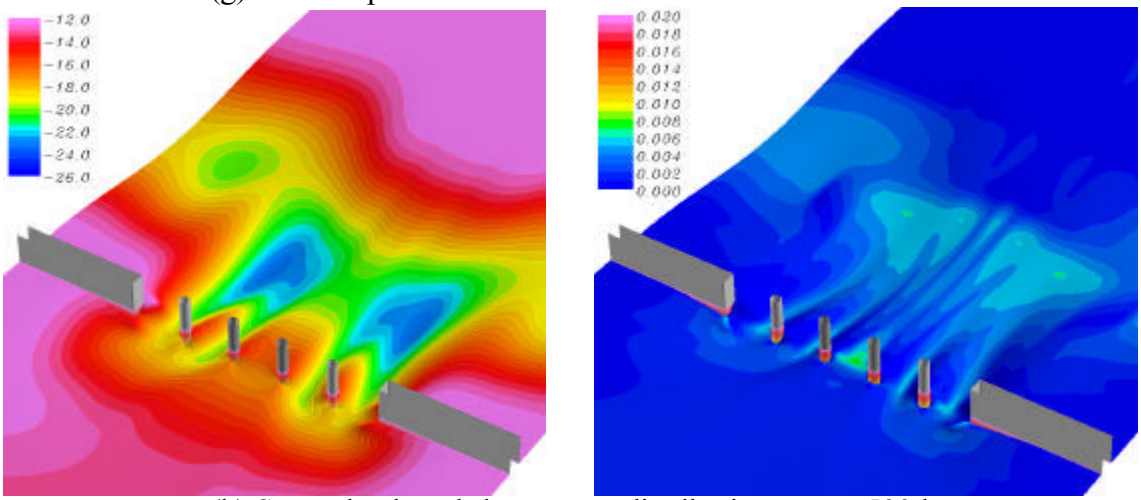


(h) Scour depth and shear stress distributions at t = 500 hr

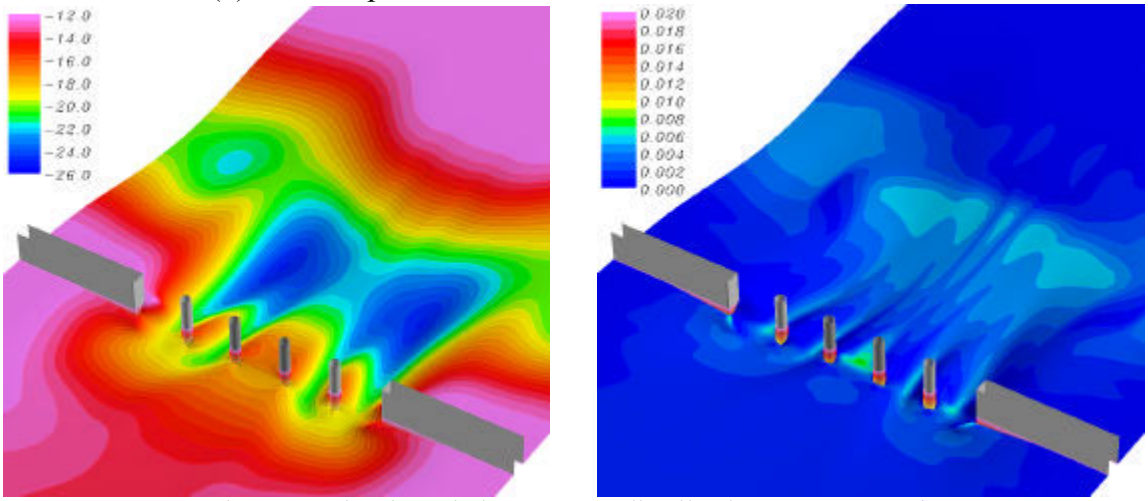


(i) Scour depth and shear stress distributions at t = 600 hr

Figure 10. Continued: (g) t = 400 hr, (h) t = 500 hr, (i) t = 600 hr

For completeness, we shall examine also the change in shear stresses as the scour hole developed. It is interesting to note that the shear stress decays rather slowly for the present configuration. It took about 45 hours for the maximum bed shear stress to drop from the initial 20.2 $N/m^2$ down to 10 $N/m^2$. A detailed examination of the time history indicated that the maximum shear stress actually increases slightly between t = 100 hr and 125 hr in the region between the two middle piers. This is most likely caused by a change in scour hole shape and an increase of local flow velocity while the flow was re-directed through the bridge. After t = 125 hr, the shear stress continued to decrease slowly while the scour hole deepened at a significantly faster rate. At the end of the simulation (t = 600 hr), the maximum shear stress remains quite high at 7.49 $N/m^2$ or about 7.5 times of the critical shear stress. The maximum scour depth is –13.1 m (–25.1 m below the free surface). Since the bed shear stress is still above critical shear stress in the bottom of the scour hole, it is anticipated that a much longer simulation time will be needed in order to attain the ultimate scour depth under the present flow conditions. However, if our primary interest is to determine the ultimate scour depth, then it is possible to use a larger slope for the scour rate equation so that the final scour depth can be obtained much more quickly.

Finally, it should be emphasized that the scour rate, in general, is a nonlinear function of the shear stress and must be determined experimentally. It is also important to note that the scour rate may also depend on other fluid flow characteristics such as the turbulence structure, vortex shedding, or pressure gradients. In order to further improve the predictive capability of the present method, it is necessary to develop a more general scour rate equation for more accurate representation of the erodibility function for cohesive soils.

## SUMMARY AND CONCLUSIONS

A chimera RANS method has been employed in conjunction with a scour rate equation for the simulation of scour process in cohesive soils around two complex pier configurations. The method successfully resolved many important flow features for contraction and local scours around complex piers. The contraction and local scour patterns were found to depend on the abutment length, pier sharp, and pier spacing. To further improve the predictive capability of the present method, it is important to obtain an accurate critical shear stress and scour rate equation through laboratory experiments.

## ACKNOWLEDGEMENTS

Many organizations and individuals have contributed to the development of the scour research program at Texas A&M University. They are all thanked sincerely. Texas DOT, NCHRP, Maryland SHA, North Carolina DOT, Minnesota DOT, Illinois DOT, Texas Transportation Institute, Humboldt, Jean-Louis Briaud, Francis Ting, Ya Li, Jun Wang, Prahoro Nurtjahyo, Kiseok Kwak, Yiwen Cao, Seung-Woon Han, Rao Gudavalli, Suresh Perugu, Gengshen Wei, Peter Smith, Tony Schneider, Melinda Luna, Kim Culp, Jay Vose, Tom Dahl, David Stolpa, Mark McClelland, John Delphia, Andy Kosicki, Stan

Davis, John Boynton, Ryhad Wahad, Bill Moore, Steven Smith, Larry Arneson, Daryl Greer, Robert Henthorne, Richard Phillips, Mehmet Tumay, Sterling Jones, Tim Hess, Mahir Al-Nadaf.

## REFERENCES

1. Chen, H.C., 1995a, "Submarine Flows Studied by Second-Moment Closure," Journal of Engineering Mechanics, Vol. 121, No. 10, pp. 1136-1146, October 1995.
2. Chen, H.C., 1995b, "Assessment of a Reynolds Stress Closure Model for Appendage-Hull Junction Flows," Journal of Fluids Engineering, Vol. 117, No. 4, pp. 557-563.
3. Chen, H.C., Briaud, J.-L., Ting, F.C.K., Wei, G., Gudavalli, R. and Perugu, S., 1999, "Numerical Simulation of Scour Processes Around a Prototype Pier Under Flood Conditions," Proceedings of the 13th ASCE Engineering Mechanics Conference, Johns Hopkins University, Baltimore, MD.
4. Chen, H.C. and Chen, M., 1998, "Chimera RANS Simulation of a Berthing DDG-51 Ship in Translational and Rotational Motions," International Journal of Offshore and Polar Engineering, Vol. 8, No. 3, pp. 182-191.
5. Chen, H.C. and Korpus, R., 1993, "A Multi-block Finite-Analytic Reynolds-Averaged Navier-Stokes Method for 3D Incompressible Flows," ASME FED-Vol. 150, pp. 113-121, ASME Fluids Engineering Conference, Washington, D.C..
6. Chen, H.C., Lin, W.M., and Hwang, Y.W., 2002a, "Validation and Application of Chimera RANS Method for Ship-Ship Interactions in Shallow Water and Restricted Waterway," Proceedings, 24th Symposium on Naval Hydrodynamics, Fukuoka, Japan.
7. Chen, H.C., Liu, T., and Huang, E.T. 2002b, "Time-Domain Simulation of Large Amplitude Ship Roll Motions by a Chimera RANS Method," International Journal of Offshore and Polar Engineering, Vol. 12, No. 3, pp. 206-212.
8. Chen, H.C., Liu, T., Huang, E.T. and Davis, D.A., 2000, "Chimera RANS Simulation of Ship and Fender Coupling for Berthing Operations," International Journal of Offshore and Polar Engineering, Vol. 10, No. 2, pp. 112-122.
9. Chen, H.C. and Patel, V.C., 1988, "Near-Wall Turbulence Models for Complex Flows Including Separation," AIAA Journal, Vol. 26, No. 6, pp. 641-648.
10. Chen, H.C., Patel, V.C. and Ju, S., 1990, "Solutions of Reynolds-Averaged Navier-Stokes Equations for Three-Dimensional Incompressible Flows," Journal of Computational Physics, Vol. 88, No. 2, pp. 305-336.
11. Du, X., 1997, "Numerical Simulation of Three-Dimensional Flow Field and Local Scour at Bridge Crossings." Ph.D. Dissertation, The University of Mississippi.
12. Li, Y., 2002, private communications.
13. Olsen, N. R. B., 1996, "Three-dimensional numerical modeling of local scour," Hydroinformatics'96, Zurich, Switzerland.
14. Olsen, N. R. B. and Melaaen, M.C. (1993), "Three-dimensional calculation of scour around cylinders," Journal of Hydraulic Engineering, Vol. 119, No. 9, pp. 1048-1054.
15. Roulund, A., 2000, "Three-dimensional Numerical Modeling of Flow Around a Bottom-Mounted Pile and Its Application to Scour," Ph.D. Thesis, Technical University of Denmark.